



Article

Removal of Arsenic from Wastewater Using Hydrochar Prepared from Red Macroalgae: Investigating its Adsorption Efficiency and Mechanism

Aisha Khan Khanzada ¹, Muhammad Rizwan ^{2,*}, Hussein E. Al-Hazmi ^{1,*} , Joanna Majtacz ¹,
Tonni Agustiono Kurniawan ³  and Jacek Mąkinia ^{1,*}

- ¹ Department of Sanitary Engineering, Faculty of Civil and Environmental Engineering, Gdańsk University of Technology, ul. Narutowicza 11/12, 80-233 Gdańsk, Poland; aiskhanz@pg.edu.pl (A.K.K.); joamajta@pg.edu.pl (J.M.)
- ² Center for Advanced Studies in Water, Mehran University of Engineering and Technology, Hyderabad 76062, Pakistan
- ³ College of the Environment and Ecology, Xiamen University, Xiamen 361102, China
- * Correspondence: drmrizwan.uspcasw@faculty.muett.edu.pk (M.R.); hussein.hazmi1@pg.edu.pl (H.E.A.-H.); jmakinia@pg.edu.pl (J.M.)

Abstract: Arsenic (As) is a prominent carcinogen component produced via both geogenic and anthropogenic processes, posing serious risks to human health. This study aimed to investigate the potential of hydrochar prepared from red macroalgae for removing As from synthetic wastewater. The hydrochar was produced through 5 h hydrothermal carbonization (HTC) treatment at 200 °C, and then, chemically activated with ferric chloride hexahydrate (FeCl₃·6H₂O). SEM analysis revealed a permeable structure of hydrochar, while FTIR analysis detected the occurrence of several functional groups at the hydrochar interface. EDS analysis showed an increase in carbon concentration after FeCl₃·6H₂O activation. Hydrochar was then tested in batch experiments to investigate its As removal efficiency, with ICP-MS used to determine the levels of As after the adsorption process. The results showed that As removal efficiency increased with increasing initial As concentration from 50 to 250 mg/L, and the highest As removal efficiency was 84.75% at a pH of 6, initial concentration of 0.25 mg/L, and adsorbent dose of 1000 mg at 120 min. The Langmuir isotherm model supported the occurrence of homogeneous adsorption over the surface of hydrochar, while the pseudo-second-order model confirmed the chemisorptive nature of the process.

Keywords: hydrothermal carbonization; macroalgae; arsenic removal; activated hydrochar; Langmuir and pseudo models; wastewater treatment



Citation: Khanzada, A.K.; Rizwan, M.; Al-Hazmi, H.E.; Majtacz, J.; Kurniawan, T.A.; Mąkinia, J. Removal of Arsenic from Wastewater Using Hydrochar Prepared from Red Macroalgae: Investigating its Adsorption Efficiency and Mechanism. *Water* **2023**, *15*, 3866. <https://doi.org/10.3390/w15213866>

Academic Editor: Antonio Zuerro

Received: 5 October 2023

Revised: 1 November 2023

Accepted: 3 November 2023

Published: 6 November 2023



Copyright: © 2023 by the authors. Licensee MDPI, Basel, Switzerland. This article is an open access article distributed under the terms and conditions of the Creative Commons Attribution (CC BY) license (<https://creativecommons.org/licenses/by/4.0/>).

1. Introduction

Achieving optimal wastewater treatment for reuse depends on several factors, including the initial wastewater quality, the intended use of the treated water, local regulations, and available resources [1–4]. Despite these variables, there are standard steps and technologies commonly used in wastewater reuse. These methods encompass biological treatments, such as conventional and anammox-based systems, as well as advanced oxidation techniques like ozonation or UV/H₂O₂ [5–8]. Furthermore, advanced membrane processes, including reverse osmosis, nanofiltration, and ultrafiltration, are also widely utilized.

Arsenic (As) is a highly toxic element that occurs in more than 200 mineral varieties [9]. Natural events, such as volcanic eruptions, flooding, and soil erosion, and human activities, such as irrigation, mining, and pesticide usage, contribute to its presence in the environment [10,11]. As exists in two forms: organic and inorganic. The dominant forms of organic As are arseno-sugars, dimethyl-arsenic acid, and monomethyl-arsenic acid, and they can be found in shellfish as a product of biological processes in surface water. Inorganic arsenic

forms, such as arsenate As (V) and arsenite As (III), can commonly be found in natural water sources [12]. The intake of arsenic-contaminated water can have severe health consequences, including cancer, cardiovascular disease, and reproductive effects. To mitigate these effects, the World Health Organization recommends a limit of 10 $\mu\text{g/L}$ of As in drinking water [13]. Pfeiffer et al. recorded that five out of 54 drinking water samples had arsenic levels exceeding the World Health Organization (WHO)'s maximum permissible limit, with a maximum recorded concentration of 300 $\mu\text{g L}^{-1}$ of arsenic in the drinking water samples [14]. Shahid et al.'s study documented that the mean groundwater arsenic (As) content reported in 43 studies was 120 $\mu\text{g/L}$, with a range from 0.1 $\mu\text{g/L}$ to 2090 $\mu\text{g/L}$. It also noted that about 73% of the mean As content values in these studies exceeded the World Health Organization (WHO)'s permissible limit of 10 $\mu\text{g/L}$ for drinking water, while 41% exceeded the permissible limit of 50 $\mu\text{g/L}$ for arsenic in Pakistan [15]. Research has shown a link between the risk of congenital heart disease and maternal exposure to arsenic in drinking water, even when the exposure levels are low [16,17].

Conventional methods for removing As from drinking and wastewater include adsorption, coagulation/precipitation, membrane methods, ion exchange, and lime softening, with adsorption being the most effective [18]. However, cost remains a significant challenge in the widespread implementation of adsorption methods [12]. To overcome this challenge, natural materials, such as olive core, peat, and algae, have been used as low-cost adsorbents to remove heavy metal ions from wastewater [19]. In addition, thermochemical processes can transform biomass into high-carbon-content products, such as charcoal, which can also be used as adsorbents [20].

Hydrothermal carbonization (HTC) is a promising technology that transforms low-calorie biomass into carbon-based solids known as hydrochar [21]. The process is carried out at specific retention times (0.5–24 h) and pressures (2–10 MPa) and relatively low temperatures (180–350 °C) [22,23]. Unlike other processes, HTC can transform biomass into hydrochar without an energy-intensive drying phase. In addition, underwater biomass is a valuable source as it requires less agricultural land and yields higher biomass production. This carbon product can be transformed into various biofuels through microbial activity or thermochemical processes [24].

Biochar, especially hydrochar, has emerged as a favored adsorbent in environmental cleanup efforts [25]. Biochar can be divided into two categories: pyrochar and hydrochar. Pyrochar is produced through the pyrolysis of dried biomass under specific conditions such as optimal temperatures, heating rates, and retention times [26]. Activation techniques can improve the physical and chemical properties of pyrochar, including its specific surface area, surface functional groups, and pore structures, making it more effective for applications such as As (V) adsorption [27,28]. For instance, magnetic MnFe_2O_4 -engineered pyrochar has an As (V) adsorption capacity of 90 mg/g [29], and zirconium-iron-modified pyrochar can remove As (V) with a capacity of 62.5 mg/g [30]. On the other hand, hydrochar is synthesized through the HTC of wet biomass and has specific functional groups, such as carboxyl and hydroxyl [31]. However, its limited surface area and dispersed porous structures can reduce its effectiveness. Therefore, activations, such as sulfonation, magnetization, oxidation, and ammoniation, are essential to improving the comprehensive functionalities of hydrochar [32]. Although hydrochar has successfully been used in various organic or inorganic contaminant treatment processes, research on its ability to remove As contamination has been limited [31]. Further studies are necessary to fully evaluate the renewability of hydrochar-based adsorbent materials. Ref. [33] evaluated the ability of hydrochars derived from olive pomace oil to adsorb As. The effect of FeCl_3 activation and additional hydrothermal treatment was assessed at various pH values, and the impact of solution pH on the stability and production of hydrochar was analyzed. The results showed that while alkaline HTC decreased the stability of the adsorbent, it improved As (V) adsorption to 4.1 mg/g, and the iron coating of the adsorbent [34].

The purpose of this research is to determine the ability of macroalgae-based hydrochar as a sustainable resource to eliminate As from wastewater. Macroalgae, distinct from

microalgae, possess plant-like attributes with higher protein content and a composition rich in cellulose, lignin, and hemicellulose. Several studies have explored the potential of hydrothermal carbonization (HTC) as an environmentally friendly and versatile technique for sustainable biomass processing. Biller and Ross (2012) investigated the application of HTC for producing biochar, biocrude, and syngas from algal biomass, showcasing its versatility in converting various biomass sources [35]. Patel et al. (2021) addressed ecological issues caused by waste seaweed through HTC, emphasizing the circular green solution of producing hydrochar and nutrient-rich liquid slurry from the seaweed [36]. Rasam et al. (2021) examined the impact of different parameters on the HTC process for *Sargassum horneri* macroalgae and used machine learning techniques to estimate key process parameters [37]. Spagnuolo et al. (2023) furthered the exploration of HTC by investigating hydrochar recovery from *Sargassum muticum* macroalgae and assessing its potential in adsorbing organic water pollutants for environmental remediation [38]. Spagnuolo, Bressi et al. (2023) explored the practical applications of HTC solutions by investigating the reuse of discarded liquid phases as seed-priming treatments for *Phaseolus vulgaris* L., highlighting the benefits of HTC in agriculture and resource management [39]. The utilization of macroalgae offers a sustainable and renewable resource, and has promising applications in hydrochar, biofuels, and bioproducts, potentially transforming the sustainable landscape [20]. In this study, we explored the novel application of macroalgae-based hydrochar for arsenic removal, a previously unexplored avenue. Our findings reveal macroalgae-based hydrochar's promising potential as an effective method for mitigating arsenic contamination in wastewater. The hydrochar was produced through biosynthesis and was thoroughly characterized before being chemically activated with $\text{FeCl}_3 \cdot 6\text{H}_2\text{O}$. $\text{FeCl}_3 \cdot 6\text{H}_2\text{O}$ is a well-known chemical activator for hydrochar due to its iron content, and can introduce functional groups and surface modifications to the hydrochar, making it more effective in adsorbing contaminants like arsenic (As). Zhang et al.'s study focuses on creating an arsenic (As) adsorption material called iron-modified hydrochar using hydrothermal carbonization (HTC) with different iron species: $\text{FeCl}_3 \cdot 6\text{H}_2\text{O}$, $\text{FeSO}_4 \cdot 7\text{H}_2\text{O}$, and $\text{Fe}(\text{NO}_3)_3 \cdot 9\text{H}_2\text{O}$. It investigates their physicochemical properties, iron retention stability, and As adsorption capabilities [40]. Ghanizadeh et al. used iron chloride as a chemical activator to impregnate activated carbon with iron because iron impregnation is a well-known and effective method for enhancing the adsorption properties of activated carbon [41]. Iron impregnation can significantly improve activated carbon's ability to remove various contaminants, including arsenic, from water. The presence of iron on activated carbon's surface introduces active sites that can chemically bind with the target contaminants. These active sites enhance the adsorption capacity and efficiency of the activated carbon [42]. To evaluate its proficiency in extracting arsenic (As) from a liquid solution and to explore the impact of variables like pH, temperature, and initial As concentration, we carried out comprehensive kinetic and equilibrium studies. These investigations delved into the adsorption process, examining its control through both chemical and physical adsorption mechanisms. The results of this study have important implications for the potential use of macroalgae-based hydrochar as a sustainable resource for removing As from contaminated water sources.

2. Materials and Methods

2.1. Chemicals

This study employed several materials, including Reagecon^{MT} chemicals, which are standard for ICP and ICP-MS, at a concentration of 1000 $\mu\text{g}/\text{mL}$ (1000 ppm) in 2–5% nitric acid (HNO_3). Other materials used were extra-pure ferric chloride hexahydrate ($\text{FeCl}_3 \cdot 6\text{H}_2\text{O}$), citric acid monohydrate, and sodium hydroxide (NaOH), as well as additional HNO_3 .

2.2. Preparation of Hydrochar (HC)

The complete process of hydrochar preparation and activation is illustrated in Figure S1 in the Supplementary Materials file. Red macroalgae was collected from the beach near

Katti Kund, Gharo, in Krachi, Sidnh, Pakistan. The samples were thoroughly cleaned using tap water and distilled water, and then, dried at room temperature for 48 h. The dried samples were then ground and sieved to obtain particles greater than 600 μm in size [43].

To produce hydrochar, a Teflon-lined stainless-steel reactor with a 100 mL capacity was used. The hydrochar was produced through the HTC process. A catalytic solution of 40 mg of citric acid (monohydrate) was mixed with 50 mL of distilled water, and 10 g of dried algal sample was added to the solution. The mixture was then added to an autoclave and placed in a preheated oven for 5 h at 200 °C. After 5 h, the carbon product was washed, filtered, and dried for an additional 5 h at 120 °C. The final hydrochar product was weighed.

2.3. Activation of Hydrochar

The hydrochar was activated using iron (III) chloride hexahydrate ($\text{FeCl}_3 \cdot 6\text{H}_2\text{O}$). To prepare a solution, 4.98 g of $\text{FeCl}_3 \cdot 6\text{H}_2\text{O}$ was dissolved in 30 mL of distilled water and mixed thoroughly. Hydrochar (3 g) was then added to the solution, and the pH was maintained between 7 and 7.5. The mixture was placed in an electronic shaker and agitated at 200 rpm for 24 h to provide sufficient time for activation. After 24 h, the solution was centrifuged for 30 min, the supernatant was discarded, and the activated hydrochar was filtered. The activated hydrochar was then washed 3 to 4 times with distilled water, and the pH was measured after the final wash to ensure it was free of impurities. Finally, the activated hydrochar was dried at 120 °C to obtain the final sample. Inductively coupled plasma mass spectrometry (ICP-MS) was used to identify the As level in water after treatment.

2.4. Surface Morphology and Characterization of Hydrochar (HC) and Activated Hydrochar (AHC) Samples

Scanning Electron Microscope (SEM) imaging and Energy-Dispersive X-ray Spectroscopy (EDS) analysis were performed using a Hitachi S-4800 Field Emission SEM build with an EDS analysis feature on the hydrochar sample to observe its surface and identify its elemental composition, respectively. In SEM, an electron beam is focused on the sample surface to generate an image of the sample, while EDS helps in determining the elemental composition by analyzing the X-ray signals produced by the sample. FTIR spectroscopy was also performed using a Nicolet™ iS20 FTIR Spectrometer to identify the functional groups present in the sample. Infrared radiation in the range of approximately 10,000 to 100 cm^{-1} was directed towards the sample, and the adsorbed energy was transformed into vibrational energy. This was then detected as a spectrum between 4000 cm^{-1} and 400 cm^{-1} , providing a molecular fingerprint of the sample and offering insights into its functional groups.

2.5. Batch Adsorption

A batch test was used to evaluate As removal efficiency using hydrochar as an adsorbent. The batch test was carried out in 15 mL falcon tubes at a temperature of 25 °C. The solutions of 0.1 M nitric acid and 0.1 M sodium hydroxide were used to maintain the pH of the test solution at 2, 4, 6, 8 and 10. A 0.25 mg/L concentration of As with a fixed amount of adsorbent (magnetized hydrochar) dose of 0.01 g was used in all experiments. The study employed a range of time intervals (30, 60, 90, 120, and 150 min) to observe the kinetics of the adsorption process. Varied arsenic concentrations (0.05, 0.1, 0.15, 0.2, and 0.25 mg/L) were introduced to assess the impact of initial concentration on removal efficiency. Additionally, different dosages of the adsorbent (200 mg, 400 mg, 600 mg, 800 mg, and 1000 mg) were employed in separate experiments to examine their influence.

In a batch test, the adsorption process is allowed to reach equilibrium, and the amount of contaminant adsorbed onto the surface of the adsorbent is measured. This information can then be used to evaluate the adsorption capacity and kinetics of the adsorbent and to determine the optimal conditions for removing the contaminant from the solution.



2.6. Calculations

The amount of As adsorbed, q_t , was calculated using Equation (1).

$$q_t = (C_o - C_t) * \frac{V}{m} \quad (1)$$

where q_t is the amount of As adsorbed at time t (mg/g), C_o is the initial As concentration (mg/L), C_t is the As concentration at time t (mg/L), V is the As solution volume (mL), and m is the adsorbent mass (mg).

The As removal efficiency, η_{As} , was calculated using Equation (2) as follows:

$$h_{As} = \left(C_o - \frac{C_i}{C_o} \right) * 100 \quad (2)$$

where C_o is the initial As concentration (mg/L), and C_i is the As concentration remaining at the end of reaction (mg/L).

2.6.1. Isotherm Models

To study the equilibrium adsorption of As, the Langmuir and Freundlich isotherm models were used. Equation (3) for the Langmuir isotherm model is given below:

$$\frac{1}{q_e} = \frac{1}{K_L \cdot q_{max} \cdot C_e} + \frac{1}{q_{max}} \quad (3)$$

where q_e is the quantity of heavy metal adsorbed per unit weight of adsorbent (mg/g), C_e is the equilibrium concentration (mg/L), K_L is the Langmuir adsorption parameter/constant (L/mg), and q_{max} is the maximum adsorption capacity (mg/g). Equation (4) for the Freundlich adsorption isotherm model is as follows:

$$\log q_e = \log K_f + 1/(n \cdot \log C_e) \quad (4)$$

where q_e is the quantity of heavy metal adsorbed per unit weight of adsorbent (mg/g), C_e is the equilibrium concentration (mg/L), K_f is the Freundlich constant (adsorbent's relative adsorption capacity (mg/g), and $1/n$ is the adsorption intensity.

2.6.2. Kinetic Models

The pseudo-first- and pseudo-second-order models were applied to describe the kinetics of As removal and explain the differences in the kinetic rates. According to [44], Equation (5) for the pseudo-first-order model can be written as follows:

$$\ln(q_e - q_t) = \ln q_e - K_1 * t \quad (5)$$

where q_e is the amount of heavy metal adsorbed at equilibrium (mg/g), q_t is the amount of heavy metal adsorbed at time t (mg/g), and K_1 is the pseudo-first-order rate constant.

Equation (6) for the pseudo-second-order model is presented as follows:

$$t/q_t = 1/K_2 q_e^2 + t/q_e \quad (6)$$

where K_2 is the pseudo-second-order rate constant.

Equation (7) for the intra-particle diffusion model is presented as follows:

$$q_t = K_{diff} t^{1/2} + C \quad (7)$$

q_t is the amount of arsenic adsorbed at time t ;
 K_{diff} is the intra-particle diffusion rate constant;
 C is the intercept.

3. Results

3.1. SEM Analysis of Hydrochar

SEM photographs of the hydrochar and activated hydrochar samples with a magnification of $\times 1000$ are shown in Figure 1a,b, respectively. The images highlight that a variety of pores appeared on the surface of the hydrochar due to the evaporation of the chemical activator. A similar porous structure and rough topography of carbon samples after chemical activation was reported by [45]. Likewise, Petrović et al. [46] also found similar disorganized cracks on their samples. In contrast, the surface morphology of activated hydrochar is heterogeneous, with pores of varied diameters. Because of the pores and cracks on the surface of activated hydrochar, molecules can effortlessly clog and flow into the voids. The SEM image of activated hydrochar demonstrates that the surface is substantially smoother after the chemical activation of the sample.

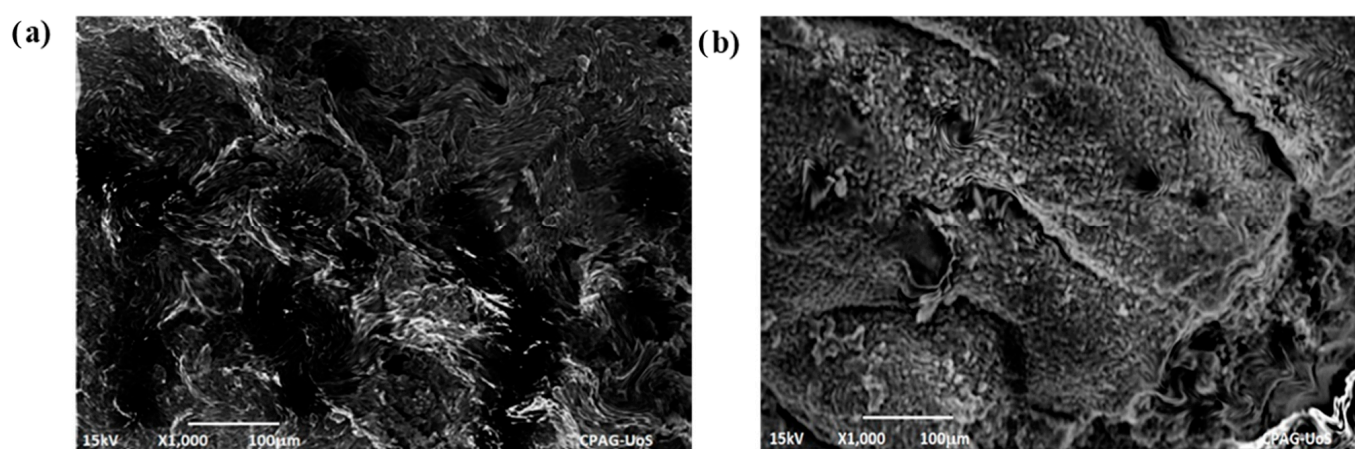


Figure 1. SEM image of adsorbent: (a) topography of hydrochar sample before activation; (b) topography of hydrochar.

3.2. Elemental Composition and Changes during Activation of Hydrochar

The EDS analysis showed that carbon and oxygen were the most abundant elements in non-activated hydrochar, constituting 34.4% and 50.6%, respectively (Figure S2a). After activation, the dominant elements in the hydrochar samples changed, and carbon, oxygen, magnesium, aluminum, silicon, nitrogen, chlorine, sulfur, phosphorus, iron, and sodium were the most abundant components, as shown in Figure S2b in the Supplementary Materials file.

Table S1 in the Supplementary Materials file shows the weight percentage and atomic weight percentage of various elements present in both the activated and non-activated samples of hydrochar. Moreover, the activation process (heating of AHC for 5 h at 120 °C) led to the appearance of chloride and iron in the hydrochar sample. The activation also increased the carbon percentage and decreased the oxygen percentage. The percentages of silicon, sulfur, and phosphorous also decreased after activation. Yan et al. [47] found that the bamboo sample they studied contained 2.0%, 23.3%, and 74. % of Mn, O, and C, respectively. The presence of silicon and other elements in hydrochar samples has also been reported in other studies [48]. Ma et al. [49], produced hydrochar from lignin and reported the availability of 57.6% carbon and 8.9% oxygen in their sample.

3.3. Identification and Impact of Surface Functional Groups of HC, AHC during As Adsorption, and AHC after As Adsorption

The functional groups on the surface of hydrochar (HC), activated hydrochar (AHC), and activated hydrochar after As adsorption (AHC+As) were identified using the FTIR approach, and the results are presented in Figure 2. The spectra of HC, AHC, and AHC+As were found to be similar. C-H stretching vibrations were present between 2755 cm^{-1} and

2990 cm^{-1} , and C-H bending was observed at a peak of 1970 cm^{-1} . The peak level at and C-O stretching vibration bands at 1124 cm^{-1} and 1455 cm^{-1} were detected. These findings are consistent with previous studies, such as Lei et al. [50], who identified similar functional groups in hydrochar derived from *Salix* biomass. Figure 2 also highlights that after activation, the Fe-O group was also present as a peak at 570 cm^{-1} .

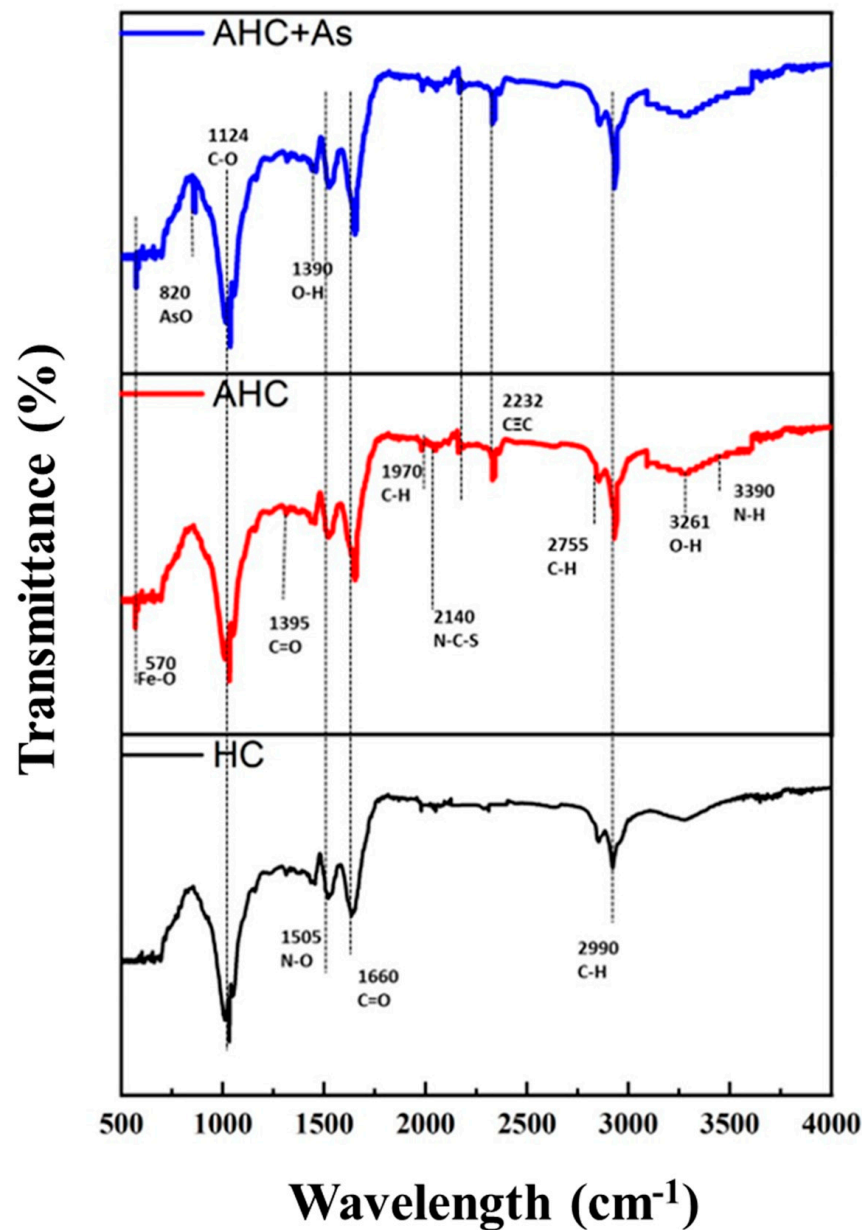


Figure 2. FTIR adsorption spectra: hydrochar sample before activation, FTIR spectra of hydrochar sample after activation, and activated hydrochar spectra after As adsorption.

The functional groups present on the surface of hydrochar after the chemical activation are shown in Figure 2. The peak 3261 cm^{-1} indicated the occurrence of O-H stretches, and the peak at 1390 cm^{-1} was attributed to the tensile bonding of OH, which is likely due to the adsorption of water on the surface of nanoparticles [51,52]. The C=O and COO stretching peaks were likely linked to carboxyl groups, which can enhance resistance to alkaline conditions [53]. The curves at 1501–1510, 3390, and 2140 cm^{-1} , respectively, indicated N=O stretching, N-H bending, and N-C-S stretching, respectively. Correspondingly, C=O stretching and C=C stretching were observed as peaks at 1395, 1660, and 2232 cm^{-1} , respectively.



The presence of functional groups, including hydroxyl, carboxyl, and amide, enhances As adsorption [54]. The availability of certain organic acid functional groups, such as OH or COO^- , may contribute to the variation in As adsorption trends [55]. Kumar and Jiang [56] provided evidence that the availability of amine, hydroxyl, and carboxyl functional groups increased after the activation of their sample, which contributed to As adsorption. Similarly, in this study, the presence of amine, hydroxyl, and carboxyl functional groups increased after activation, significantly improving As adsorption.

3.4. Factors Affecting As Removal

3.4.1. Effect of pH

The availability of binding sites on the adsorbent surface is dependent on the pH of the solution, with hydrogen ions having a strong affinity for heavy metal ions, which can affect their binding to the adsorbent [57,58]. In this study, the effects of pH on the As adsorption capacity of activated hydrochar was investigated. As removal efficiency was measured at pH levels ranging from 2 to 10, and the findings are presented in Figure 3a. The results show that the neutral pH was most effective in removing As, at 150 min of equilibrium time, 200 rpm shaking speed, a pH of 6.5, an As concentration of 0.25 mg/L, and a hydrochar dosage of 1000 mg/L. The pH graph reveals that as the pH increased from 2 to 6, the removal efficiency and adsorption capacity rose significantly by 49% and 77%, respectively. However, at a pH of 10, the efficiency and adsorption capacity decreased.

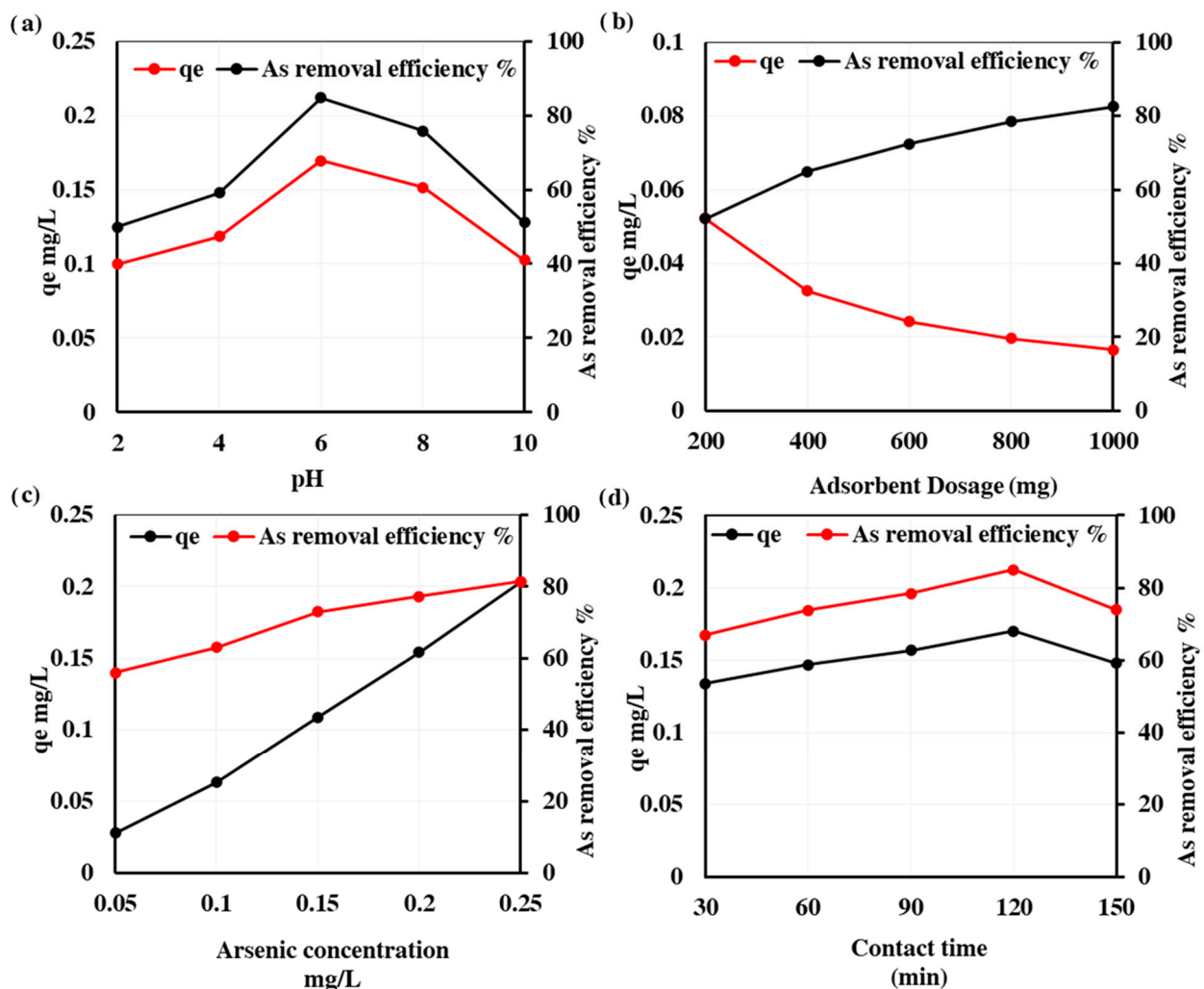


Figure 3. Factors affecting the As removal efficiency of AHC: (a) effect of pH, (b) effect of AHC (adsorbent) dosage, (c) effect of As concentration, (d) effect of contact time.

Previous studies have reported similar optimal pH ranges for As removal. Kamala et al. [59] found that the efficacy of As removal by fresh biomass was dependent on a pH range of 6 to 8, with the optimal adsorption taking place at a pH of 6. Likewise, Abtahi et al. [60] found that maximum As (IV) adsorption was achieved at a pH of 6. However, it is important to note that the optimal pH range may vary depending on the adsorbent material and the experimental conditions.

3.4.2. Effect of Adsorbent Dosage

The following experiment aimed to determine the effect of adsorbent dosage, ranging from 200 to 1000 mg, on the efficiency of As removal and the adsorption capacity of As by activated hydrochar. According to the results presented in Figure 3b, the efficiency was increased from 52.5% to 82% with an increase in adsorbent dosage, while the adsorption rate of As (adsorption capacity) shows an inverse relationship with the adsorbent dosage. The graph shows that the maximum adsorption capacity occurred at 1g. This trend in the experiment shows that an increased amount of adsorbent provides more binding sites, which enhances the sorption mechanism and improves the efficiency of As removal [61]. Rahmani et al. [62] suggested a suitable dosage of 1 g/L for As adsorption experiments.

3.4.3. Effect of Initial As Concentration

The purpose of this experiment was to investigate the adsorption behavior of an adsorbent at different As concentrations, ranging from 0.5 mg/L to 0.25 mg/L, under a constant adsorbent dosage of 1000 mg. As shown in Figure 3c, the As removal efficiency and removal capacity of the adsorbent increased as the As concentration increased. It was predicted that the low initial concentration of As limited the possibility of collision between the adsorption sites of the adsorbent and As, resulting in a lower As removal efficiency. However, with increasing initial As concentrations, the difference in concentration became greater, which led to a higher adsorption capacity and a faster rate of As removal [63]. A similar pattern was investigated in Christobel's batch study [64].

3.4.4. Effect of Contact Time

The purpose of this experiment was to investigate the effect of contact time on the As removal efficiency and adsorption capacity of activated hydrochar. The results are presented in Figure 3d, which shows that the As removal efficiency increased from 67% to 85.05%, while the adsorption capacity improved to 0.1701 mg/g. The maximum adsorption was achieved at 120 min. Mandal et al. also found that 120 min was the optimal time for removing As [65]. In contrast, Q. Li et al. [66] examined the efficiency of two different adsorbents, magnesia-loaded fly ash cenospheres (MGLC) and manganese-loaded fly ash cenospheres (MNLC), for As removal. The equilibrium point for MNLC adsorption was reached after 120 min. As removal typically occurs in stages, with the initial stage being quick. As the contact time passes, the rate of removal slows until equilibrium is reached. The monolayer and fast adsorption are probably caused by ion exchange or physical adsorption on the surface of the adsorbent. However, as time passes, fewer active sites become available, and competition from existing metal ions slows down the adsorption rate due to fewer binding sites [67].

The findings of this research are consistent with the study of Dudek and Koodyska [68], who concluded that 120 min is an appropriate duration to achieve As removal equilibrium [68]. Attinti et al. [69] also used silicon nanoparticles covered with goethite and achieved equilibrium at 120 min.

3.5. Equilibrium Investigation

Adsorption is a process that involves interactions between adsorbate and adsorbent molecules, as well as between these molecules and the solvent. Of the five types of processes that can occur during adsorption, the adsorbent-adsorbate interaction is particularly important, as it must be maximized in order for the adsorption operation to take place [70].

The equilibrium properties of heavy metal adsorption on the adsorbent surface can be determined using the Langmuir and Freundlich isotherm models [71]. Figure 4a shows a graph of $1/q_e$ vs. $1/C_e$, which was used to derive the Langmuir isotherm model, determine the value of q_{max} , and obtain the experimental data. The Freundlich isotherm was used to determine whether surface adsorption was heterogeneous or multilayer [72]. The value of K_f was estimated using experimental data from the Freundlich isotherm model and a graph of $\log Q_e$ vs. $\log C_e$, as shown in Figure 4b. Table 1 provides the calculated values for the constants in both models. In this study, the Langmuir model was followed because the R^2 value of the Langmuir model was 0.981 and q_{max} was 3.8314 mg/g, whereas the R^2 of the Freundlich model was 0.9173, which is less than the R^2 value of Langmuir model, indicating that surface adsorption was not multilayer or heterogeneous.

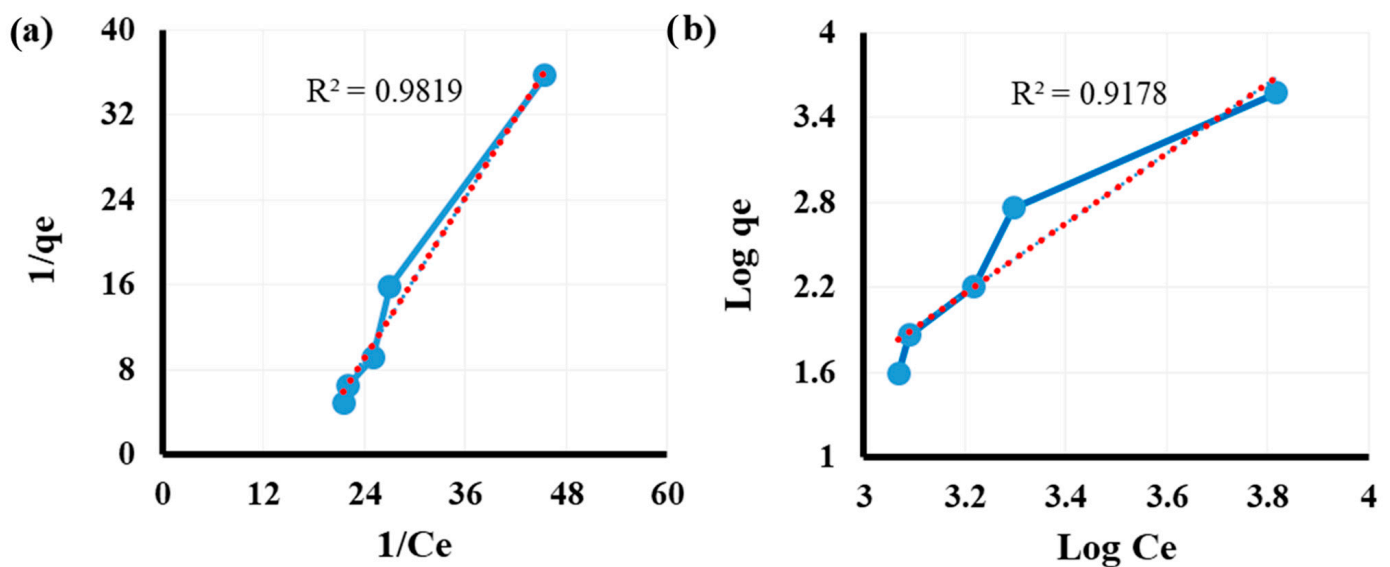


Figure 4. Equilibrium investigation: (a) Langmuir isotherm model; (b) Freundlich isotherm model.

In a study by Altundoğan et al. [73], red mud was used as an adsorbent for As removal from an aqueous solution. The results showed that the Langmuir isotherm could successfully model the adsorption behavior of As on the red mud. The Langmuir isotherm assumes that adsorption occurs on a homogeneous surface with a finite number of identical sites, and that there is no interaction between adsorbed molecules. In another study by Goswami et al. [74], the Langmuir isotherm was used to model the adsorption of cadmium ions on modified rice husk. The Langmuir model provided a good fit to the experimental data, indicating that the adsorption process was monolayer and homogeneous. Likewise, in a research study by Goldberg and Johnston [75], the Langmuir isotherm was used to model the adsorption of gold complexes on activated carbon. The Langmuir model provided a good fit to the experimental data and was used to determine the maximum adsorption capacity of the activated carbon.

In this study, R^2 values indicate that the Langmuir isotherm model and the metal ion elimination method strongly correlate, and suggest that biosorption had continuous adsorption energy. If the adsorbate–adsorbent interaction is stronger than the other interactions, a monolayer is formed. The first adsorbed molecule acts as a starter for the second molecule, which is tightly bound to the first molecule in a binding site. The homogenous increase in binding sites on the biomass surface is mainly attributed to the strong correlation between the Langmuir isotherm and the findings of [76].

According to Yu et al. [77]’s study, the adsorption process of As onto adsorbents (based on multi-amino-functionalized cellulose) is best described by the Langmuir model, which suggests that it is a monolayer adsorption process. The Langmuir model also provides the maximum adsorption capacities (Q_{max}) for As (III) and As (V), which are 5.71 mg/g and

75.13 mg g⁻¹, respectively. Chaudhry et al. [78] demonstrated that when the temperature of the solution was increased from 27 to 45 °C, the Langmuir adsorption capacity of IZBOCS for As (V) showed a significant increase from 45.05 to 84.75 mg g⁻¹. The feasibility of the adsorption process was indicated by the separation factor values, which were 0.435, 0.489, and 0.508 at 27 °C, 35 °C, and 45 °C, respectively. Moreover, Cheng et al. [79] used iron oxide nanoparticles for As removal and highlighted that the sorption isotherms were found to be well described by the Langmuir equation, which yielded a maximum sorption capability of 83 mg g⁻¹ for As (V) at a pH of 3 and 42 mg g⁻¹ for As (III) at a pH of 7. The adsorption process on FG2 was found to follow a pseudo-second-order kinetic model and was well fitted in the Langmuir isotherm, with a maximum adsorption capacity of 69.44 mg g⁻¹ at a pH of 3 [80]. Correspondingly, other studies that used different materials for As adsorption and for which adsorption fitted the Langmuir isotherm are mentioned in Table 1.

Table 1. Summary of kinetic constant values of Langmuir isotherm model and Freundlich isotherm model.

Material	As Species	Langmuir Isotherm Model Parameters			Freundlich Isotherm Model Parameters			References
		KL (L/mg)	Q max (mg/g)	R ²	K F (mg/g)	N	R ²	
Activated hydrochar	As (III/V)	0.0123	3.8314	0.981	0.031	0.403	0.917	This study
Multi-amino-functionalized cellulose	As (III)	0.21	5.71	0.970	2.11	3.94	0.926	[77]
	As (V)	0.078	75.13	0.992	26.85	5.02	0.934	
Iron–zirconium binary oxide-coated sand (27, 35 and 45 °C)	As (V)	0.0104	45.05	0.957	1.19	1.7	0.997	[78]
	As (V)	0.0083	66.22	0.856	1.10	1.5	0.999	
	As (V)	0.0077	84.75	0.955	1.15	1.3	0.997	
Iron oxide nanoparticles	As (III)	0.4	42	0.978	11.3	2.1	0.921	[79]
Iron oxide nanoparticles	As (V)	0.8	83	0.998	28.6	3.1	0.828	
Magnetic graphene oxide nanocomposites	As (V)	0.385	69.44	0.905	26.57	4.787	0.819	[80]
Iron oxide nanoparticles	As (V)	0.11	28.57	–	2.6	0.68	–	[81]
Magnetic gelatin-modified biochar	As (V)	0.81	43.15	0.89	19.27	0.24	0.70	[82]
Phosphorus (P)-modified biochar (PLBC) (Taraxacum mongolicum Hand-Mazz)	As (III)	0.08	30.76	0.843	6.76	0.33	0.818	[83]
Ultisol	As (V)	137.3	24.27	0.995	31.3	5.00	0.997	
Ultisol + biochar	As (V)	66.4	21.51	0.996	26.1	4.67	0.995	
Ultisol + biochar derived from aluminum-treated rice straw	As (V)	77.0	25.97	0.994	38.8	3.62	0.992	[84]
Ultisol + aluminum-treated biochar form rice straw	As (V)	185.5	26.95	0.996	42.9	4.08	0.988	
Rice-husk biochar-stabilized iron and copper oxide nanoparticles	As (III/V)	0.19	20.32	0.555	2.84	1.28	0.975	[85]

3.6. Kinetic Study

Three different kinetic models, the pseudo-first-order, pseudo-second-order, and intra-particle diffusion models, were examined in this study. Table 2 provides the kinetic constant values obtained from the first- and second-order and intra-particle diffusion models. These models are commonly used in solid–liquid systems [85]. In the past, numerous studies have been conducted that investigate hydrochar performance based on kinetic models using

first- and second-order and intra-particle diffusion models for the removal of different heavy metals and other contaminants [86–88]. As shown in Figure 5a, plotting $\ln(q_e - qt)$ against time (t) yielded the experimental data for the pseudo-second-order model and K1 values. Figure 5b demonstrates a relationship between t/q_e and time (t) to compute pseudo-second-order experimental data and the value of k2 (Table 2). The intra-particle diffusion model is often employed to gain insights into the adsorption process and to determine if it is controlled by intra-particle diffusion. This model is the primary rate-limiting step. The qt versus \sqrt{t} plot should exhibit a linear relationship, starting from the origin with a small C value. Figure 5c investigates an intra particle diffusion model within the studied medium, from which we derived critical parameters to assess the process. The R_2 yielded a value of 0.61899, indicating the model's ability to explain approximately 61.899% of the variance in the adsorption data. The diffusion rate constant (k diff) was measured at 0.00322, representing the rate at which adsorption occurs, with an associated uncertainty of ± 0.00146 . 'C', serving as the intercept in our adsorption equation, was determined to be 0.17051, with an uncertainty of ± 0.01383 . These findings provide fundamental insights into the adsorption process within the medium and highlight the role of the intercept 'C' in our adsorption equation, despite this not being a modest fit of the model to the data. Further investigation and potential model refinement may be required to improve the goodness of fit. The determination coefficient (R_2) value was 0.9567, while the R_2 value for the pseudo-second-order model was 0.9913, indicating that the pseudo-second-order model was more suitable for this study than the pseudo-first-order model. The higher R_2 values suggest that the pseudo-second-order model more accurately predicted the experimental data obtained during the investigation of the kinetics of As adsorption on macroalgae-based hydrochar than the pseudo-first-order model. This suggests that the As (III) elimination process in the studied system is chemical rather than physical. In addition, Goldberg and Johnston [75] observed that their results also followed the second-order model.

Table 2. Summary of kinetic constant values of pseudo-first-order model and pseudo-second-order model.

Materials	As Species	Pseudo-First-Order Model Parameters			Pseudo-Second-Order Model Parameters			Intra-Particle Diffusion Model Parameters			References
		K1 (min^{-1})	qe. Cal. (mg/g)	R^2	K2 ($\text{mg g}^{-1} \text{min}^{-1}$)	qe. Cal. (mg/g)	R^2	K(diff) ($\text{mg g}^{-1} \text{min}^{-1/2}$)	C (mg/g)	R^2	
Activated hydrochar	As (III/V)	−0.0053	0.078	0.9567	2.3452	0.156	0.991	0.00322	0.17051	0.6189	This study
Untreated red-mud biochar	As (V)	1.195	451.4	0.983	0.00357	482.9	0.987	0.062	0.233	0.6664	
Red-mud-modified biochar	As (V)	1.446	1656.5	0.900	0.00126	1758.6	0.957	0.212	0.9087	0.7298	
Untreated red-mud biochar	As (III)	0.805	296.0	0.948	0.00366	319.5	0.960	0.048.95	0.115	0.7662	[86]
Red-mud-modified biochar	As (III)	0.686	377.9	0.911	0.00236	412.0	0.927	0.6657	0.132	0.8842	
Iron oxide nanoparticles	As (V)	0.50	0.66	0.92	4.3	4.0	0.99	N.A.	N.A.	N.A.	[81]
Phosphorus (P)-modified biochar (PLBC)/Taraxacum mongolicum Hand-Mazz	As (III)	0.23 ± 0.028	16.3 ± 0.4	0.972	0.020 ± 0.002	17.1 ± 0.4	0.997	N.A.	N.A.	N.A.	[83]
Magnetic gelatin-modified biochar	As (V)	0.03	26.64	0.87	0.00142	28.389	0.92	N.A.	N.A.	N.A.	[82]



Table 2. Cont.

Materials	As Species	Pseudo-First-Order Model Parameters			Pseudo-Second-Order Model Parameters			Intra-Particle Diffusion Model Parameters			References
		K1 (min ⁻¹)	qe. Cal. (mg/g)	R ²	K2 (mg g ⁻¹ min ⁻¹)	qe. Cal. (mg/g)	R ²	K(diff) (mg g ⁻¹ min ^{-1/2})	C (mg/g)	R ²	
Magnetic Fe ₃ O ₄ /Douglas fir biochar composites	As (III)	N.A.	N.A.	N.A.	0.337	1.30	0.9960	N.A.	N.A.	N.A.	
Magnetic Fe ₃ O ₄ /Douglas fir biochar composites	As (III)	N.A.	N.A.	N.A.	0.319	3.75	0.9999	N.A.	N.A.	N.A.	[87]
Magnetic Fe ₃ O ₄ /Douglas fir biochar composites	As (III)	N.A.	N.A.	N.A.	0.049	6.15	0.9894	N.A.	N.A.	N.A.	
Rice-husk biochar-stabilized iron and copper oxide nanoparticles	As (III/V)	0.17	1.75	0.839	0.09	6.84	0.999				[85]

Note: N.A. = Non-available.

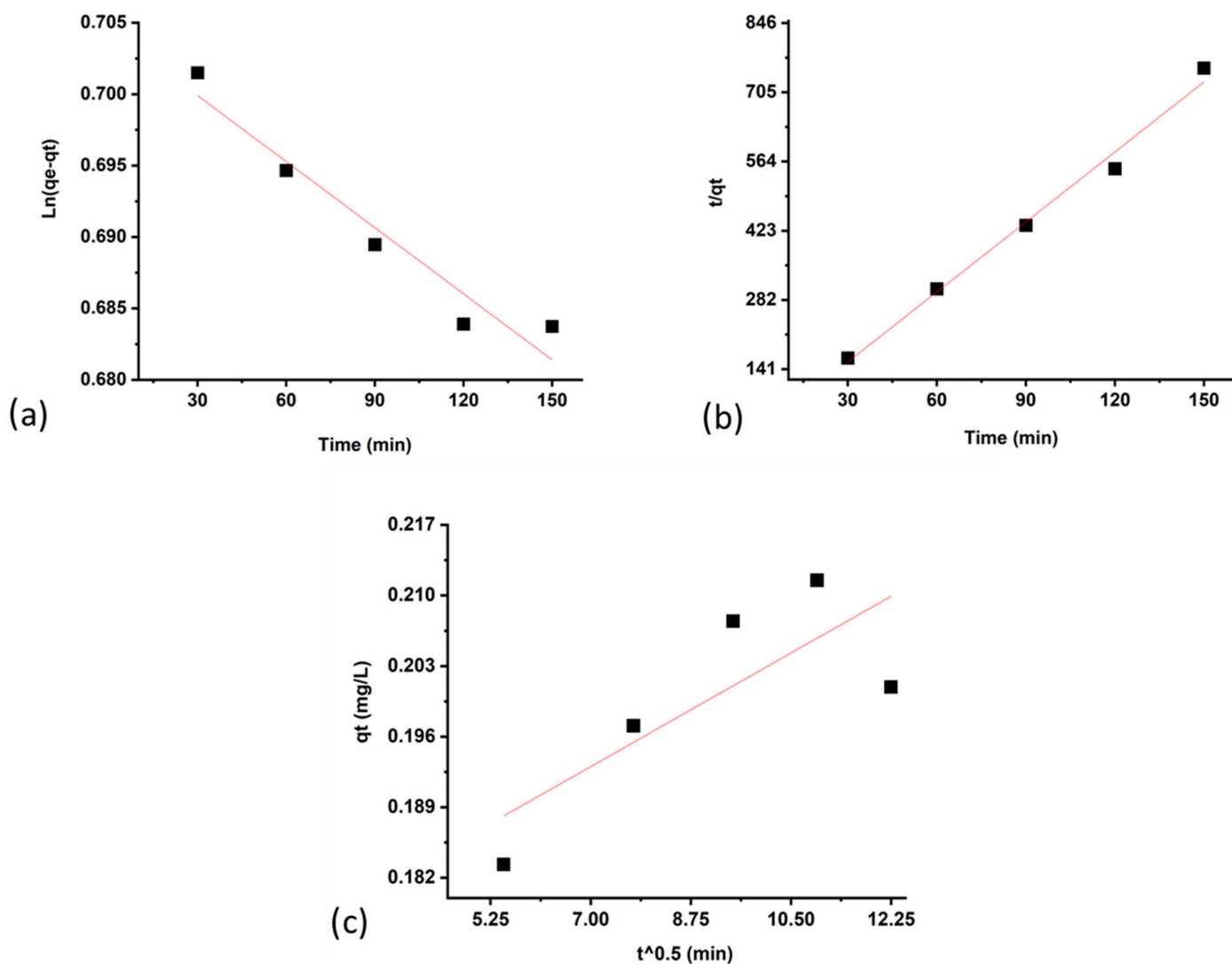


Figure 5. Kinetic study: (a) pseudo-first-order model; (b) pseudo-second-order model; (c) intra-particle diffusion model.

Wu et al. [86] investigated the correlation coefficients of different kinetic models for different materials. The results show that the pseudo-first-order kinetics had low correlation

coefficients ($R^2 < 0.9$), which was considered unfavorable. On the other hand, the pseudo-second-order model had very high correlation coefficients ($R^2 \geq 0.99$) for all the data examined. In another study based on the fit coefficient ($R^2 = 0.913$), it was determined that the pseudo-second-order model was a good fit for the adsorption process. This indicated that the rate-limiting step in the process was the chemisorption of As (V), which involved a chemical interaction between As (V) ions and polar functional groups on the adsorbent, such as ion exchange and the chelating reaction [81]. Also, Navarathna et al. [87] made composites of Magnetic Fe_3O_4 and Douglas fir biochar (MBC), and showed that the adsorption kinetics data were most accurately represented by the pseudo-second-order model, with an R^2 value greater than 0.99.

The use of both biochar@Fe and biochar@Cu in combination effectively removes As and can be accurately represented by the pseudo-second-order kinetic model. This model assumes that each As ion is associated with two M-OH centers during the chemical adsorption reaction. Because the concentration of As ions is lower than the number of available metal hydroxyl active sites (M-OH), the overall reaction rate can be approximated by a pseudo-second-order reaction [85]. Ahmed et al. [83] investigated phosphorus (P)-modified biochar (PLBC) for As adsorption. The pseudo-first-order kinetic model appeared to fit well (with $R^2 = 0.97$), but it underestimated the adsorption rate in the first 20 min. On the other hand, the pseudo-second-order kinetic model provided a slightly better fit to the experimental data, with an R^2 value of 0.99. These results suggest that the overall adsorption process may be influenced by electron exchange or sharing between the sorbent and sorbate, indicating that chemisorption could be the rate-limiting step. Similarly, other studies that used different materials for As adsorption that fitted the pseudo-second-order model are mentioned in Table 2.

4. As Removal Mechanisms

Figure 6 shows the mechanism of As adsorption in hydrochar, which is believed to be primarily through surface complexation [88]. The activated hydrochar has a high surface area and a porous structure, which provides numerous active sites for chemical interactions. The active sites are primarily located on the surface of the hydrochar, where they can interact with contaminants in the surrounding environment. Wang et al. [89] synthesized two types of biochar composites using pinewood biochar and Ni/Mn oxides or Ni/Mn-layered double hydroxides. The first type was produced via the pyrolysis of pinewood biochar (NMMF) with Ni/Mn oxides, while the second type was produced via the precipitation of Ni/Mn-layered double hydroxides onto the pinewood biochar (NMMB) using $\text{MnCl}_2 \cdot 4\text{H}_2\text{O}$ and $\text{Ni}(\text{NO}_3)_2 \cdot 6\text{H}_2\text{O}$. The As (V) removal efficiency of NMMB and NMMF was tested using a 12 mg/L As (V) solution, and the results showed that NMMB had higher efficiency at 98% compared to NMMF, which had 10.6% removal efficiency. Both modified biochars showed an improved maximum As (V) sorption capacity compared to the unmodified biochar, with NMMB having a capacity of 6.520 g/kg and NMMF having a capacity of 0.549 g/kg [89]. Figure 6 illustrates the potential mechanisms responsible for the immobilization of As on the activated hydrochar surfaces. In contrast, Alkurdi et al. [88] observed that the point of zero charge for activated hydrochar was a solution pH of higher than 8, which resulted in a positively charged surface of the hydrochar. This positively charged surface facilitated strong electrostatic forces between As (V) and the surface.

When As comes into contact with the hydrochar surface, it can form strong chemical bonds with functional groups, such as carboxyl (HCOO), hydroxyl (-OH), and amino (-NH₂) groups [90]. These functional groups can act as electron donors and can form a complex with the As through a process known as ligand exchange (Figure 6). The complex formed by hydrochar and As is believed to be stable and can remain in place for a long time. As can interact with these electrons, forming a stable complex. The understanding of these mechanisms has been applied to the development of activated biochar materials for water remediation. For instance, the incorporation of nano-zero-valent iron (Fe_0) into biochar can improve the immobilization of As (V) in water by creating strong chemisorption



interactions through an oxidation and reduction reaction on the surface of the biochar [88]. To investigate the binding mechanism between As and AHC, we conducted a comparison of FTIR spectra before and after adsorption, as illustrated in Figure 2. In Figure 2, we also compared the FTIR spectra of AHC and HC prior to the adsorption of arsenic ions. All three materials displayed broad adsorption bands at 1395 and 1660 cm^{-1} , which can be attributed to the vibrations of C=O bonds [91]. Notably, this adsorption bands exhibited minimal changes following arsenic adsorption, suggesting that the O-H and the C=O bond were not significant contributors to the adsorption process.

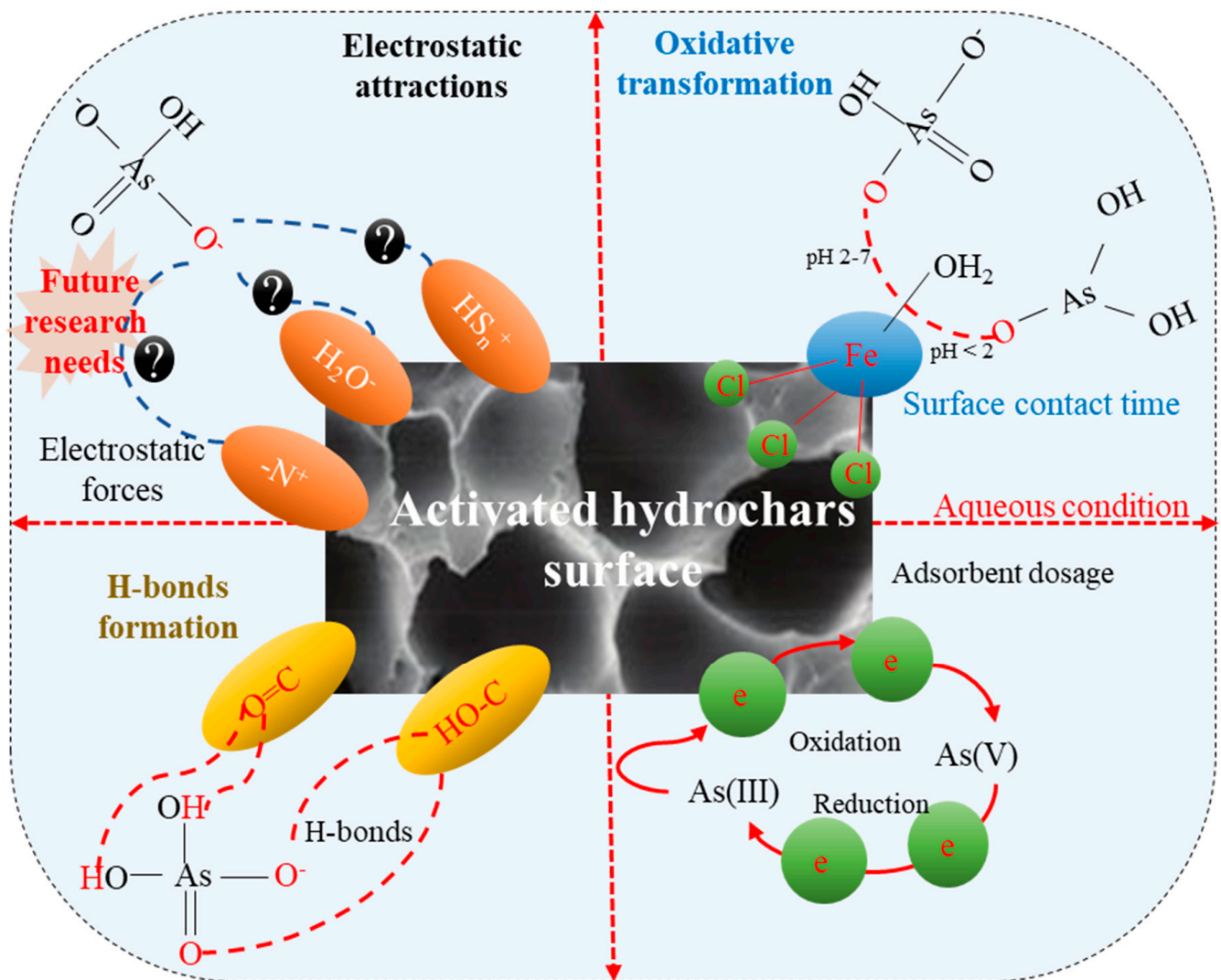


Figure 6. Schematic of potential mechanisms for the adsorption of As on activated hydrochar surface [52,88,90].

Simultaneously, we observed the appearance of a prominent and well-defined peak at 820 cm^{-1} , mainly associated with As-O. These symmetric and asymmetric As-O vibrations within the Fe structure imply the formation of iron arsenate precipitation on the material's surface [92,93].

5. Future Outlook and Perspectives Trends

1. The removal of As from wastewater using activated hydrochar extracted from macroalgae has been shown to be a highly effective method. The increasing demand for sustainable and cost-effective methods for treating As-contaminated wastewater is driving the growth of this technology. Macro-algae are abundant and could be

harvested in large quantities, making them an attractive option for the production of hydrochar. In addition, the production process is low-cost and energy-efficient, making it an attractive option for small-scale operations.

2. Another research direction should be the development of advanced techniques for the activation of hydrochar, such as chemical, thermal, and microwave activation. These techniques could improve the adsorption capacity and efficiency of hydrochar, making it an even more practical solution for As removal from wastewater.
3. It is expected that the use of activated hydrochar extracted from macro-algae will continue to grow as the demand for sustainable and effective methods for treating As-contaminated wastewater increases. In addition, the development of new and improved methods for the activation of hydrochar and the use of other sustainable materials for the production of hydrochar is expected to drive the growth of this technology in the future.

Overall, the future outlook and trends of As removal from wastewater by activated hydrochar extracted from macro-algae are very positive. This technology is expected to play an increasingly important role in addressing the challenge of As contamination in wastewater.

6. Conclusions

Hydrochar extracted from red macroalgae is a suitable adsorbent for As adsorption after activation with $\text{FeCl}_3 \cdot 6\text{H}_2\text{O}$. Our SEM results revealed a smoother surface and an increase in porous areas after hydrochar activation, providing As with a larger surface area to adsorb. FTIR analysis showed the presence of amines, hydroxyl, and carboxyl functional groups, which played an essential role in improving As adsorption. Our EDS results indicated the presence of carbon and oxygen due to the burning process and the presence of Fe and Cl after activation. The batch experiments showed that the optimum pH level for As removal was 6.0, and increasing the adsorbent dosage enhanced the As removal efficiency from 52.5% to 82%, but the rate of As adsorption (adsorption capacity) was not improved. Furthermore, the variation in initial As concentration affected the adsorption process. This study best followed the Langmuir isotherm model, indicating the formation of a monolayer over the adsorbent's surface. The kinetic study showed that the pseudo-second-order model best fit the experimental data, suggesting that chemical bonding took place between the contaminant and the functional group present on the surface of the activated hydrochar surface.

Supplementary Materials: The following supporting information can be downloaded at: <https://www.mdpi.com/article/10.3390/w15213866/s1>, Figure S1. Systematic diagram to prepare hydrochar and activate hydrochar with $\text{FeCl}_3 \cdot 6\text{H}_2\text{O}$; Figure S2. Elemental spectra of the hydrochar sample before activation (a) and after activation (b). Note: S (sulfur), C (carbon), N (nitrogen), O (oxygen), Fe (iron), Na (sodium), Mg (magnesium), Al (aluminum), Si (silicon), P (phosphorus), Cl (chlorine); Table S1. Element compound weight and atomic weight percentage of hydrochar and activated hydrochar sample.

Author Contributions: All authors contributed to the study conception and design. Material preparation and data collection and analysis were performed by A.K.K. and H.E.A.-H. The first draft of the manuscript was written by A.K.K., H.E.A.-H., J.M. (Joanna Majtacz) and T.A.K. The final manuscript was written and revised by M.R. and J.M. (Jacek Małania). All authors commented on previous versions of the manuscript. All authors have read and agreed to the published version of the manuscript.

Funding: This research received no external funding.

Data Availability Statement: The data and materials are available upon request.

Conflicts of Interest: This study was conducted in line with the Helsinki Declaration. All authors participated the work, and read and approved the final manuscript. All the authors agree to publish it. The authors have no relevant financial or non-financial conflict of interest to disclose.

References

- Al-Hazmi, H.E.; Mohammadi, A.; Hejna, A.; Majtacz, J.; Esmaeili, A.; Habibzadeh, S.; Saeb, M.R.; Badawi, M.; Lima, E.C.; Maĳinia, J. Wastewater Reuse in Agriculture: Prospects and Challenges. *Environ. Res.* **2023**, *236*, 116711. [\[CrossRef\]](#)
- Al-Hazmi, H.E.; Hassan, G.K.; Maktabifard, M.; Grubba, D.; Majtacz, J.; Maĳinia, J. Integrating Conventional Nitrogen Removal with Anammox in Wastewater Treatment Systems: Microbial Metabolism, Sustainability and Challenges. *Environ. Res.* **2022**, *215*, 114432. [\[CrossRef\]](#)
- Joseph, T.M.; Al-Hazmi, H.E.; Śniatała, B.; Esmaeili, A.; Habibzadeh, S. Nanoparticles and Nanofiltration for Wastewater Treatment: From Polluted to Fresh Water. *Environ. Res.* **2023**, *238*, 117114. [\[CrossRef\]](#)
- Afify, A.A.; Hassan, G.K.; Al-Hazmi, H.E.; Kamal, R.M.; Mohamed, R.M.; Drewnowski, J.; Majtacz, J.; Maĳinia, J.; El-Gawad, H.A. Electrochemical Production of Sodium Hypochlorite from Salty Wastewater Using a Flow-by Porous Graphite Electrode. *Energies* **2023**, *16*, 4754. [\[CrossRef\]](#)
- Al-Hazmi, H.E.; Lu, X.; Grubba, D.; Majtacz, J.; Badawi, M.; Maĳinia, J. Sustainable Nitrogen Removal in Anammox-Mediated Systems: Microbial Metabolic Pathways, Operational Conditions and Mathematical Modelling. *Sci. Total Environ.* **2023**, *868*, 161633. [\[CrossRef\]](#)
- Al-Hazmi, H.E.; Shokrani, H.; Shokrani, A.; Jabbour, K.; Abida, O.; Mousavi Khadem, S.S.; Habibzadeh, S.; Sonawane, S.H.; Saeb, M.R.; Bonilla-Petriciolet, A.; et al. Recent Advances in Aqueous Virus Removal Technologies. *Chemosphere* **2022**, *305*, 135441. [\[CrossRef\]](#)
- Al-Hazmi, H.E.; Kot-Wasik, A.; Shokrani, A.; Majtacz, J.; Vatanpour, V.; Munir, M.T.; Habibzadeh, S.; Hejna, A.; Hasanpour, M.; Mohammadi, A.; et al. Diving Boldly into COVID-19 Contaminated Wastewater: Eyes at Nanotechnology-Assisted Solutions. *Clin. Transl. Discov.* **2023**, *3*, e195. [\[CrossRef\]](#)
- Al-Hazmi, H.E.; Maktabifard, M.; Grubba, D.; Majtacz, J.; Hassan, G.K.; Lu, X.; Piechota, G.; Mannina, G.; Bott, C.B.; Maĳinia, J. An Advanced Synergy of Partial Denitrification-Anammox for Optimizing Nitrogen Removal from Wastewater: A Review. *Bioresour. Technol.* **2023**, *381*, 129168. [\[CrossRef\]](#)
- Bhardwaj, A.; Rajput, R.; Misra, K. Chapter 9—Status of Arsenic Remediation in India. In *Advances in Water Purification Techniques*; Ahuja, S., Ed.; Elsevier: Amsterdam, The Netherlands, 2019; pp. 219–258. ISBN 978-0-12-814790-0.
- Algieri, C.; Pugliese, V.; Coppola, G.; Curcio, S.; Calabro, V.; Chakraborty, S. Arsenic Removal from Groundwater by Membrane Technology: Advantages, Disadvantages, and Effect on Human Health. *Groundw. Sustain. Dev.* **2022**, *19*, 100815. [\[CrossRef\]](#)
- Khatun, J.; Intekhab, A.; Dhak, D. Effect of Uncontrolled Fertilization and Heavy Metal Toxicity Associated with Arsenic(As), Lead(Pb) and Cadmium (Cd), and Possible Remediation. *Toxicology* **2022**, *477*, 153274. [\[CrossRef\]](#)
- Vasireddy, D. Arsenic Adsorption onto Iron-Chitosan Composite from Drinking Water. Ph.D. Thesis, University of Missouri, Columbia, MO, USA, 2005.
- Hashmi, M.Z.; Ahmed, Z.; Rehman, S.U.; Reka, A.A. A Review on Arsenic Status in Environmental Compartments from Pakistan. *Arab. J. Geosci* **2023**, *16*, 130. [\[CrossRef\]](#)
- Pfeiffer, M.; Batbayar, G.; Hofmann, J.; Siegfried, K.; Karthe, D.; Hahn-Tomer, S. Investigating Arsenic (As) Occurrence and Sources in Ground, Surface, Waste and Drinking Water in Northern Mongolia. *Environ. Earth Sci.* **2015**, *73*, 649–662. [\[CrossRef\]](#)
- Shahid, M.; Niazi, N.K.; Dumat, C.; Naidu, R.; Khalid, S.; Rahman, M.M.; Bibi, I. A Meta-Analysis of the Distribution, Sources and Health Risks of Arsenic-Contaminated Groundwater in Pakistan. *Environ. Pollut.* **2018**, *242*, 307–319. [\[CrossRef\]](#)
- Pezeshki, H.; Hashemi, M.; Rajabi, S. Removal of Arsenic as a Potentially Toxic Element from Drinking Water by Filtration: A Mini Review of Nanofiltration and Reverse Osmosis Techniques. *Heliyon* **2023**, *9*, e14246. [\[CrossRef\]](#)
- Fu, D.; Kurniawan, T.A.; Li, H.; Wang, H.; Wang, Y.; Li, Q. Co-Oxidative Removal of Arsenite and Tetracycline Based on a Heterogeneous Fenton-like Reaction Using Iron Nanoparticles-Impregnated Biochar. *Environ. Pollut.* **2021**, *290*, 118062. [\[CrossRef\]](#)
- Ghorbanzadeh, N.; Jung, W.; Halajnia, A.; Lakzian, A.; Kabra, A.N.; Jeon, B.-H. Removal of Arsenate and Arsenite from Aqueous Solution by Adsorption on Clay Minerals. *Geosyst. Eng.* **2015**, *18*, 302–311. [\[CrossRef\]](#)
- De Gisi, S.; Lofrano, G.; Grassi, M.; Notarnicola, M. Characteristics and Adsorption Capacities of Low-Cost Sorbents for Wastewater Treatment: A Review. *Sustain. Mater. Technol.* **2016**, *9*, 10–40. [\[CrossRef\]](#)
- Khan Khanzada, A.; Al-Hazmi, H.E.; Śniatała, B.; Muringayil Joseph, T.; Majtacz, J.; Abdulrahman, S.A.M.; Albaseer, S.S.; Kurniawan, T.A.; Rahimi-Ahar, Z.; Habibzadeh, S.; et al. Hydrochar-Nanoparticle Integration for Arsenic Removal from Wastewater: Challenges, Possible Solutions, and Future Horizon. *Environ. Res.* **2023**, *238*, 117164. [\[CrossRef\]](#)
- Yoganandham, S.T.; Sathyamoorthy, G.; Renuka, R.R. Chapter 8—Emerging Extraction Techniques: Hydrothermal Processing. In *Sustainable Seaweed Technologies*; Advances in Green and Sustainable Chemistry; Torres, M.D., Kraan, S., Dominguez, H., Eds.; Elsevier: Amsterdam, The Netherlands, 2020; pp. 191–205. ISBN 978-0-12-817943-7.
- Sharma, H.B.; Sarmah, A.K.; Dubey, B. Hydrothermal Carbonization of Renewable Waste Biomass for Solid Biofuel Production: A Discussion on Process Mechanism, the Influence of Process Parameters, Environmental Performance and Fuel Properties of Hydrochar. *Renew. Sustain. Energy Rev.* **2020**, *123*, 109761. [\[CrossRef\]](#)
- Xu, X.; Zhu, D.; Jian, Q.; Wang, X.; Zheng, X.; Xue, G.; Liu, Y.; Li, X.; Hassan, G.K. Treatment of Industrial Ferric Sludge through a Facile Acid-Assisted Hydrothermal Reaction: Focusing on Dry Mass Reduction and Hydrochar Recyclability Performance. *Sci. Total Environ.* **2023**, *869*, 161879. [\[CrossRef\]](#)
- Liu, Y.; Zhou, S.; Fu, Y.; Sun, X.; Li, T.; Yang, C. Characterization of Dissolved Organic Matter in Biochar Derived from Various Macroalgae (Phaeophyta, Rhodophyta, and Chlorophyta): Effects of Pyrolysis Temperature and Extraction Solution pH. *Sci. Total Environ.* **2023**, *869*, 161786. [\[CrossRef\]](#)

25. Yameen, M.Z.; AlMohamadi, H.; Naqvi, S.R.; Noor, T.; Chen, W.-H.; Amin, N.A.S. Advances in Production & Activation of Marine Macroalgae-Derived Biochar Catalyst for Sustainable Biodiesel Production. *Fuel* **2023**, *337*, 127215. [[CrossRef](#)]
26. Xia, C.; Cai, L.; Zhang, H.; Zuo, L.; Shi, S.Q.; Lam, S.S. A Review on the Modeling and Validation of Biomass Pyrolysis with a Focus on Product Yield and Composition. *Biofuel Res. J.* **2021**, *8*, 1296–1315. [[CrossRef](#)]
27. Panahi, H.K.S.; Dehhaghi, M.; Ok, Y.S.; Nizami, A.-S.; Khoshnevisan, B.; Mussatto, S.I.; Aghbashlo, M.; Tabatabaei, M.; Lam, S.S. A Comprehensive Review of Engineered Biochar: Production, Characteristics, and Environmental Applications. *J. Clean. Prod.* **2020**, *270*, 122462. [[CrossRef](#)]
28. Yek, P.N.Y.; Peng, W.; Wong, C.C.; Liew, R.K.; Ho, Y.L.; Wan Mahari, W.A.; Azwar, E.; Yuan, T.Q.; Tabatabaei, M.; Aghbashlo, M.; et al. Engineered Biochar via Microwave CO₂ and Steam Pyrolysis to Treat Carcinogenic Congo Red Dye. *J. Hazard. Mater.* **2020**, *395*, 122636. [[CrossRef](#)]
29. Wen, Z.; Xi, J.; Lu, J.; Zhang, Y.; Cheng, G.; Zhang, Y.; Chen, R. Porous Biochar-Supported MnFe₂O₄ Magnetic Nanocomposite as an Excellent Adsorbent for Simultaneous and Effective Removal of Organic/Inorganic Arsenic from Water. *J. Hazard. Mater.* **2021**, *411*, 124909. [[CrossRef](#)]
30. Rahman, M.A.; Lamb, D.; Rahman, M.M.; Bahar, M.M.; Sanderson, P.; Abbasi, S.; Bari, A.S.M.F.; Naidu, R. Removal of Arsenate from Contaminated Waters by Novel Zirconium and Zirconium-Iron Modified Biochar. *J. Hazard. Mater.* **2021**, *409*, 124488. [[CrossRef](#)]
31. Liu, Z.; Wang, Z.; Chen, H.; Cai, T.; Liu, Z. Hydrochar and Pyrochar for Sorption of Pollutants in Wastewater and Exhaust Gas: A Critical Review. *Environ. Pollut.* **2021**, *268*, 115910. [[CrossRef](#)]
32. Sajjadi, B.; Zubatiuk, T.; Leszczynska, D.; Leszczynski, J.; Chen, W.Y. Chemical Activation of Biochar for Energy and Environmental Applications: A Comprehensive Review. *Rev. Chem. Eng.* **2019**, *35*, 777–815. [[CrossRef](#)]
33. Capobianco, L.; Di Caprio, F.; Altimari, P.; Astolfi, M.L.; Pagnanelli, F. Production of an Iron-Coated Adsorbent for Arsenic Removal by Hydrothermal Carbonization of Olive Pomace: Effect of the Feedwater pH. *J. Environ. Manag.* **2020**, *273*, 111164. [[CrossRef](#)]
34. Chen, H.; Xu, J.; Lin, H.; Zhao, X.; Shang, J.; Liu, Z. Arsenic Removal via a Novel Hydrochar from Livestock Waste Co-Activated with Thiourea and γ -Fe₂O₃ Nanoparticles. *J. Hazard. Mater.* **2021**, *419*, 126457. [[CrossRef](#)]
35. Biller, P.; Ross, A.B. Hydrothermal Processing of Algal Biomass for the Production of Biofuels and Chemicals. *Biofuels* **2012**, *3*, 603–623. [[CrossRef](#)]
36. Patel, N.; Acharya, B.; Basu, P. Hydrothermal Carbonization (HTC) of Seaweed (Macroalgae) for Producing Hydrochar. *Energies* **2021**, *14*, 1805. [[CrossRef](#)]
37. Rasam, S.; Talebkeikhah, F.; Talebkeikhah, M.; Salimi, A.; Moraveji, M.K. Physico-Chemical Properties Prediction of Hydrochar in Macroalgae *Sargassum Horneri* Hydrothermal Carbonisation. *Int. J. Environ. Anal. Chem.* **2021**, *101*, 2297–2318. [[CrossRef](#)]
38. Spagnuolo, D.; Iannazzo, D.; Len, T.; Balu, A.M.; Morabito, M.; Genovese, G.; Espro, C.; Bressi, V. Hydrochar from *Sargassum Muticum*: A Sustainable Approach for High-Capacity Removal of Rhodamine B Dye. *RSC Sustain.* **2023**, *1*, 1404–1415. [[CrossRef](#)]
39. Spagnuolo, D.; Bressi, V.; Chiofalo, M.T.; Morabito, M.; Espro, C.; Genovese, G.; Iannazzo, D.; Trifilò, P. Using the Aqueous Phase Produced from Hydrothermal Carbonization Process of Brown Seaweed to Improve the Growth of *Phaseolus Vulgaris*. *Plants* **2023**, *12*, 2745. [[CrossRef](#)]
40. Zhang, Y.; Chen, D.; Xing, Y.; Liu, B.; Zhou, Y.; Lu, P. Role of Nitrate in the Production of Iron-Modified Hydrochar for Arsenic Removal. *Res. Sq.* **2023**. preprint. [[CrossRef](#)]
41. Ghanizadeh, G.; Ehrampoush, M.H.; Ghaneian, M.T. Application of iron impregnated activated carbon for removal of arsenic from water. *J. Environ. Health Sci. Eng.* **2010**, *7*, 145–156.
42. Park, Y.R.; Hong, S.H.; Kim, J.H.; Park, J.Y. Arsenic Removal Using the Surface Modified Granular Activated Carbon Treated with Ferric Chloride. *J. Korean Soc. Water Wastewater* **2012**, *26*, 77–85. [[CrossRef](#)]
43. Xu, Q.; Qian, Q.; Quek, A.; Ai, N.; Zeng, G.; Wang, J. Hydrothermal Carbonization of Macroalgae and the Effects of Experimental Parameters on the Properties of Hydrochars. *ACS Sustain. Chem. Eng.* **2013**, *1*, 1092–1101. [[CrossRef](#)]
44. Yuh-Shan, H. Citation Review of Lagergren Kinetic Rate Equation on Adsorption Reactions. *Scientometrics* **2004**, *59*, 171–177. [[CrossRef](#)]
45. Uçar, S.; Erdem, M.; Tay, T.; Karagöz, S. Preparation and Characterization of Activated Carbon Produced from Pomegranate Seeds by ZnCl₂ Activation. *Appl. Surf. Sci.* **2009**, *255*, 8890–8896. [[CrossRef](#)]
46. Petrović, J.T.; Stojanović, M.D.; Milojković, J.V.; Petrović, M.S.; Šoštarić, T.D.; Laušević, M.D.; Mihajlović, M.L. Alkali Modified Hydrochar of Grape Pomace as a Perspective Adsorbent of Pb²⁺ from Aqueous Solution. *J. Environ. Manag.* **2016**, *182*, 292–300. [[CrossRef](#)]
47. Yan, W.; Zhang, H.; Sheng, K.; Mustafa, A.M.; Yu, Y. Evaluation of Engineered Hydrochar from KMnO₄ Treated Bamboo Residues: Physicochemical Properties, Hygroscopic Dynamics, and Morphology. *Bioresour. Technol.* **2018**, *250*, 806–811. [[CrossRef](#)]
48. Wu, L.M.; Zhou, C.H.; Tong, D.S.; Yu, W.H.; Wang, H. Novel Hydrothermal Carbonization of Cellulose Catalyzed by Montmorillonite to Produce Kerogen-like Hydrochar. *Cellulose* **2014**, *21*, 2845–2857. [[CrossRef](#)]
49. Ma, Q.; Cui, L.; Zhou, S.; Li, Y.; Shi, W.; Ai, S. Iron Nanoparticles in Situ Encapsulated in Lignin-Derived Hydrochar as an Effective Catalyst for Phenol Removal. *Environ. Sci. Pollut. Res.* **2018**, *25*, 20833–20840. [[CrossRef](#)]
50. Lei, Y.; Su, H.; Tian, F. A Novel Nitrogen Enriched Hydrochar Adsorbents Derived from Salix Biomass for Cr (VI) Adsorption. *Sci. Rep.* **2018**, *8*, 4040. [[CrossRef](#)]
51. Hu, Q.; Liu, Y.; Gu, X.; Zhao, Y. Adsorption Behavior and Mechanism of Different Arsenic Species on Mesoporous MnFe₂O₄ Magnetic Nanoparticles. *Chemosphere* **2017**, *181*, 328–336. [[CrossRef](#)]

52. Zhang, F.; Wang, X.; Xionghui, J.; Ma, L. Efficient Arsenate Removal by Magnetite-Modified Water Hyacinth Biochar. *Environ. Pollut.* **2016**, *216*, 575–583. [[CrossRef](#)]
53. Xu, M.; Qin, Y.; Huang, Q.; Beiyuan, J.; Li, H.; Chen, W.; Wang, X.; Wang, S.; Yang, F.; Yuan, W.; et al. Arsenic Adsorption by Different Fe-Enriched Biochars Conditioned with Sulfuric Acid. *Environ. Sci. Pollut. Res.* **2022**, *30*, 16398–16407. [[CrossRef](#)]
54. Shakoor, M.B.; Niazi, N.K.; Bibi, I.; Shahid, M.; Saqib, Z.A.; Nawaz, M.F.; Shaheen, S.M.; Wang, H.; Tsang, D.C.W.; Bundschuh, J.; et al. Exploring the Arsenic Removal Potential of Various Biosorbents from Water. *Environ. Int.* **2019**, *123*, 567–579. [[CrossRef](#)]
55. Gräfe, M. Arsenic Adsorption on Iron Oxides in the Presence of Soluble Organic Carbon and the Influence of Arsenic on Radish and Lettuce Plant Development. Ph.D. Thesis, Virginia Tech, Blacksburg, VA, USA, 2002.
56. Kumar, A.S.K.; Jiang, S.-J. Chitosan-Functionalized Graphene Oxide: A Novel Adsorbent an Efficient Adsorption of Arsenic from Aqueous Solution. *J. Environ. Chem. Eng.* **2016**, *4*, 1698–1713. [[CrossRef](#)]
57. Jin, X.; Yu, C.; Li, Y.; Qi, Y.; Yang, L.; Zhao, G.; Hu, H. Preparation of Novel Nano-Adsorbent Based on Organic-Inorganic Hybrid and Their Adsorption for Heavy Metals and Organic Pollutants Presented in Water Environment. *J. Hazard. Mater.* **2011**, *186*, 1672–1680. [[CrossRef](#)]
58. Vindevoghel, P.; Guyot, A. Suspended Emulsion Copolymerization of Acrylonitrile and Methyl Acrylate. *Polym. React. Eng.* **1995**, *3*, 23–42. [[CrossRef](#)]
59. Kamala, C.T.; Chu, K.H.; Chary, N.S.; Pandey, P.K.; Ramesh, S.L.; Sastry, A.R.K.; Sekhar, K.C. Removal of Arsenic(III) from Aqueous Solutions Using Fresh and Immobilized Plant Biomass. *Water Res.* **2005**, *39*, 2815–2826. [[CrossRef](#)]
60. Abtahi, M.; Mesdaghinia, A.; Saeedi, R.; Nazmara, S. Biosorption of As(III) and As(V) from Aqueous Solutions by Brown Macroalga *Colpomenia Sinuosa* Biomass: Kinetic and Equilibrium Studies. *Desalination Water Treat.* **2013**, *51*, 3224–3232. [[CrossRef](#)]
61. Genç-Fuhrman, H.; Tjell, J.C.; McConchie, D. Adsorption of Arsenic from Water Using Activated Neutralized Red Mud. *Environ. Sci. Technol.* **2004**, *38*, 2428–2434. [[CrossRef](#)]
62. Rahmani, A.R.; Ghaffari, H.R.; Samadi, M.T. A comparative study on arsenic (III) removal from aqueous solution using nano and micro sized zero-valent iron. *J. Environ. Health Sci. Eng.* **2011**, *8*, 157–166.
63. Gao, Q.; Wang, L.; Li, Z.; Xie, Y.; He, Q.; Wang, Y. Adsorptive Removal of Pyridine in Simulation Wastewater Using Coke Powder. *Processes* **2019**, *7*, 459. [[CrossRef](#)]
64. Irshad, S.; Xie, Z.; Mehmood, S.; Nawaz, A.; Ditta, A.; Mahmood, Q. Insights into Conventional and Recent Technologies for Arsenic Bioremediation: A Systematic Review. *Environ. Sci. Pollut. Res.* **2021**, *28*, 18870–18892. [[CrossRef](#)]
65. Mandal, S.; Sahu, M.K.; Patel, R.K. Adsorption Studies of Arsenic(III) Removal from Water by Zirconium Polyacrylamide Hybrid Material (ZrPACM-43). *Water Resour. Ind.* **2013**, *4*, 51–67. [[CrossRef](#)]
66. Li, Q.; Xu, X.; Cui, H.; Pang, J.; Wei, Z.; Sun, Z.; Zhai, J. Comparison of Two Adsorbents for the Removal of Pentavalent Arsenic from Aqueous Solutions. *J. Environ. Manag.* **2012**, *98*, 98–106. [[CrossRef](#)]
67. Abdel-Ghani, N.T.; Hefny, M.; El-Chaghaby, G.A.F. Removal of Lead from Aqueous Solution Using Low Cost Abundantly Available Adsorbents. *Int. J. Environ. Sci. Technol.* **2007**, *4*, 67–73. [[CrossRef](#)]
68. Dudek, S.; Kołodyńska, D. Enhanced Arsenic(V) Removal on an Iron-Based Sorbent Modified by Lanthanum(III). *Materials* **2020**, *13*, 2553. [[CrossRef](#)]
69. Attinti, R.; Sarkar, D.; Barrett, K.R.; Datta, R. Adsorption of Arsenic(V) from Aqueous Solutions by Goethite/Silica Nanocomposite. *Int. J. Environ. Sci. Technol.* **2015**, *12*, 3905–3914. [[CrossRef](#)]
70. Patiha; Herald, E.; Hidayat, Y.; Firdaus, M. The Langmuir Isotherm Adsorption Equation: The Monolayer Approach. *IOP Conf. Ser. Mater. Sci. Eng.* **2016**, *107*, 012067. [[CrossRef](#)]
71. Gunasundari, E.; Senthil Kumar, P. Adsorption Isotherm, Kinetics and Thermodynamic Analysis of Cu(II) Ions onto the Dried Algal Biomass (*Spirulina Platensis*). *J. Ind. Eng. Chem.* **2017**, *56*, 129–144. [[CrossRef](#)]
72. Mahmoud, M.E.; Saad, E.A.; Soliman, M.A.; Abdelwahab, M.S. Synthesis and Surface Protection of Nano Zerovalent Iron (NZVI) with 3-Aminopropyltrimethoxysilane for Water Remediation of Cobalt and Zinc and Their Radioactive Isotopes. *RSC Adv.* **2016**, *6*, 66242–66251. [[CrossRef](#)]
73. Altundoğan, H.S.; Altundoğan, S.; Tümen, F.; Bildik, M. Arsenic Adsorption from Aqueous Solutions by Activated Red Mud. *Waste Manag.* **2002**, *22*, 357–363. [[CrossRef](#)]
74. Goswami, A.; Raul, P.K.; Purkait, M.K. Arsenic Adsorption Using Copper (II) Oxide Nanoparticles. *Chem. Eng. Res. Des.* **2012**, *90*, 1387–1396. [[CrossRef](#)]
75. Goldberg, S.; Johnston, C.T. Mechanisms of Arsenic Adsorption on Amorphous Oxides Evaluated Using Macroscopic Measurements, Vibrational Spectroscopy, and Surface Complexation Modeling. *J. Colloid Interface Sci.* **2001**, *234*, 204–216. [[CrossRef](#)]
76. Foroutan, R.; Peighambaroust, S.J.; Aghdasinia, H.; Mohammadi, R.; Ramavandi, B. Modification of Bio-Hydroxyapatite Generated from Waste Poultry Bone with MgO for Purifying Methyl Violet-Laden Liquids. *Environ. Sci. Pollut. Res.* **2020**, *27*, 44218–44229. [[CrossRef](#)]
77. Yu, X.; Tong, S.; Ge, M.; Wu, L.; Zuo, J.; Cao, C.; Song, W. Synthesis and Characterization of Multi-Amino-Functionalized Cellulose for Arsenic Adsorption. *Carbohydr. Polym.* **2013**, *92*, 380–387. [[CrossRef](#)]
78. Chaudhry, S.A.; Zaidi, Z.; Siddiqui, S.I. Isotherm, Kinetic and Thermodynamics of Arsenic Adsorption onto Iron-Zirconium Binary Oxide-Coated Sand (IZBOCS): Modelling and Process Optimization. *J. Mol. Liq.* **2017**, *229*, 230–240. [[CrossRef](#)]
79. Cheng, W.; Zhang, W.; Hu, L.; Ding, W.; Wu, F.; Li, J. Etching Synthesis of Iron Oxide Nanoparticles for Adsorption of Arsenic from Water. *RSC Adv.* **2016**, *6*, 15900–15910. [[CrossRef](#)]

80. Thy, L.T.M.; Thuong, N.H.; Tu, T.H.; My, N.H.T.; Tuong, H.H.P.; Nam, H.M.; Phong, M.T.; Hieu, N.H. Fabrication and Adsorption Properties of Magnetic Graphene Oxide Nanocomposites for Removal of Arsenic (V) from Water. *Adsorpt. Sci. Technol.* **2020**, *38*, 240–253. [[CrossRef](#)]
81. Saif, S.; Tahir, A.; Asim, T.; Chen, Y.; Adil, S. Polymeric Nanocomposites of Iron–Oxide Nanoparticles (IONPs) Synthesized Using Terminalia Chebula Leaf Extract for Enhanced Adsorption of Arsenic(V) from Water. *Colloids Interfaces* **2019**, *3*, 17. [[CrossRef](#)]
82. Zhou, Z.; Liu, Y.; Liu, S.; Liu, H.; Zeng, G.; Tan, X.; Yang, C.; Ding, Y.; Yan, Z.; Cai, X. Sorption Performance and Mechanisms of Arsenic(V) Removal by Magnetic Gelatin-Modified Biochar. *Chem. Eng. J.* **2017**, *314*, 223–231. [[CrossRef](#)]
83. Ahmed, W.; Mehmood, S.; Núñez-Delgado, A.; Ali, S.; Qaswar, M.; Shakoor, A.; Maitlo, A.A.; Chen, D.-Y. Adsorption of Arsenic (III) from Aqueous Solution by a Novel Phosphorus-Modified Biochar Obtained from Taraxacum Mongolicum Hand-Mazz: Adsorption Behavior and Mechanistic Analysis. *J. Environ. Manag.* **2021**, *292*, 112764. [[CrossRef](#)]
84. He, X.; Jiang, J.; Hong, Z.; Pan, X.; Dong, Y.; Xu, R. Effect of Aluminum Modification of Rice Straw–Based Biochar on Arsenate Adsorption. *J. Soils Sediments* **2020**, *20*, 3073–3082. [[CrossRef](#)]
85. Priyadarshni, N.; Nath, P.; Nagahanumaiyah; Chanda, N. Sustainable Removal of Arsenate, Arsenite and Bacterial Contamination from Water Using Biochar Stabilized Iron and Copper Oxide Nanoparticles and Associated Mechanism of the Remediation Process. *J. Water Process Eng.* **2020**, *37*, 101495. [[CrossRef](#)]
86. Wu, C.; Huang, L.; Xue, S.-G.; Huang, Y.-Y.; Hartley, W.; Cui, M.; Wong, M.-H. Arsenic Sorption by Red Mud-Modified Biochar Produced from Rice Straw. *Environ. Sci. Pollut. Res.* **2017**, *24*, 18168–18178. [[CrossRef](#)]
87. Navarathna, C.M.; Karunanayake, A.G.; Gunatilake, S.R.; Pittman, C.U.; Perez, F.; Mohan, D.; Mlsna, T. Removal of Arsenic(III) from Water Using Magnetite Precipitated onto Douglas Fir Biochar. *J. Environ. Manag.* **2019**, *250*, 109429. [[CrossRef](#)]
88. Alkurdi, S.S.A.; Herath, I.; Bundschuh, J.; Al-Juboori, R.A.; Vithanage, M.; Mohan, D. Biochar versus Bone Char for a Sustainable Inorganic Arsenic Mitigation in Water: What Needs to Be Done in Future Research? *Environ. Int.* **2019**, *127*, 52–69. [[CrossRef](#)]
89. Wang, S.; Gao, B.; Li, Y. Enhanced Arsenic Removal by Biochar Modified with Nickel (Ni) and Manganese (Mn) Oxyhydroxides. *J. Ind. Eng. Chem.* **2016**, *37*, 361–365. [[CrossRef](#)]
90. Sun, W.; Li, H.; Li, H.; Li, S.; Cao, X. Adsorption Mechanisms of Ibuprofen and Naproxen to UiO-66 and UiO-66-NH₂: Batch Experiment and DFT Calculation. *Chem. Eng. J.* **2019**, *360*, 645–653. [[CrossRef](#)]
91. Zhou, L.; Huang, Y.; Qiu, W.; Sun, Z.; Liu, Z.; Song, Z. Adsorption Properties of Nano-MnO₂–Biochar Composites for Copper in Aqueous Solution. *Molecules* **2017**, *22*, 173. [[CrossRef](#)]
92. Chen, H.; Xu, J.; Lin, H.; Wang, Z.; Liu, Z. Multi-Cycle Aqueous Arsenic Removal by Novel Magnetic N/S-Doped Hydrochars Activated via One-Pot and Two-Stage Schemes. *Chem. Eng. J.* **2022**, *429*, 132071. [[CrossRef](#)]
93. Huang, Y.; Gao, M.; Deng, Y.; Khan, Z.H.; Liu, X.; Song, Z.; Qiu, W. Efficient Oxidation and Adsorption of As(III) and As(V) in Water Using a Fenton-like Reagent, (Ferrihydrite)-Loaded Biochar. *Sci. Total Environ.* **2020**, *715*, 136957. [[CrossRef](#)]

Disclaimer/Publisher’s Note: The statements, opinions and data contained in all publications are solely those of the individual author(s) and contributor(s) and not of MDPI and/or the editor(s). MDPI and/or the editor(s) disclaim responsibility for any injury to people or property resulting from any ideas, methods, instructions or products referred to in the content.

